Preprint Title	Outstanding fuel cell performance of a fully platinum-free electrocatalysts using a cost-effective catalyst support material
Authors	Priji Chandran and Sundara Ramaprabhu
Publication Date	17 Jan 2020
Article Type	Full Research Paper
Supporting Information File 1	Priji-Supplementary Information-Beilstein Journal of Nanotechnology.doc; 1.0 MB
ORCID® iDs	Sundara Ramaprabhu - https://orcid.org/0000-0002-7960-9470

Outstanding fuel cell performance of a fully platinum-free electrocatalysts using a cost-effective catalyst support material

Priji Chandran and Sundara Ramaprabhu*

Alternative Energy and Nanotechnology Laboratory (AENL), Nano-Functional Materials and Technology Centre (NFMTC), Department of Physics, Indian Institute of Technology Madras, Chennai, Tamil Nadu, 600036, India.

*Email: ramp@iitm.ac.in

Abstract

One of the effective way to increase the electrocatalytic activity of carbon based electrocatalyst in a fuel cell is by in-situ incorporation of heteroatom into the carbon nanostructure. Herein, a cost effective catalyst support material, nitrogen rich carbon nanostructure (NCNS) with high surface area and tubular morphology was synthesized. NCNS supported palladium-alloy based electrocatalyst (Pd_3Co/NCNS) was successfully prepared and used on both sides of a fuel cell as potential alternative to expensive Pt-based electrocatalysts. The large number of nitrogen-carbon moieties present in NCNS served as anchoring sites for catalyst nanoparticles. Moreover, the tubular morphology and high surface area plays an important role in enhanced electrochemical activity of the prepared nanocomposite. The Pd-based bimetallic alloy dispersed on NCNS exhibited high activity towards both oxidation of hydrogen and reduction of oxygen in acidic medium. Thus, a fully Pt-free electrocatalyst was constructed using a cost effective electrocatalyst. The peak power density achieved using Pd_3Co/NCNS at both anode and cathode simultaneously was found to be almost 25 % of the maximum power density attained using commercial Pt/C on both sides, which is the maximum value reported so far in PEMFC without using Pt on either sides.

Keywords

Nitrogen doped carbon; Heteroatom doping; ORR activity; Non-Pt catalyst; Carbonization.

Introduction

Energy has become the major concern in this century, which must be addressed to secure the sustainability of technologies needed in daily life. To meet the future energy requirements without environmental hazards, development and utilization of renewable energy resources is neccessary. Polymer electrolyte membrane fuel cell (PEMFC) is considered to be the most promising technology for the rapidly increasing energy demand [1,2]. The main advantages of PEMFC are fast start up time, low operating temperature, high efficiency and low pollutant emission [3,4]. For the advancement of fuel cell technology, the development of efficient electrocatalyst for both anodic and cathodic reaction is of great importance [5].

One of the major challenges for commercialization of fuel cell is the high cost and scarcity of platinum (Pt), which is the most commonly used catalyst in PEMFC. It can be overcome by either alloying Pt with transition metal or replacing Pt with other elements which is having good catalytic activity. Recently, palladium (Pd) based electrocatalysts has emerged as an alternative to Pt-based system. Pd is more abundant than Pt and have good catalytic activity after Pt. Moreover, many reports are available showing better electrocatalytic performance of Pd-TM (TM = Transition metal) alloys in fuel cell application than Pd alone [6–9]. Takenaka et al. [10] showed that among various Pd-TM (TM = Fe, Cu, Ni, Co) alloys, Pd-Co/ CNT showed higher activity towards ORR reaction. Zhang et al. [5] demonstrated N-doped porous carbon encapsulated PdCo alloy as highly durable and active electrocatalysts for both oxygen reduction reaction and ethanol oxidation reaction. Moreover, the electrochemical performance of fuel cell can be further improved by effective utilization of catalyst nanoparticles by choosing a proper catalyst support material on which the nanoparticles can be homogeneously distributed without agglomeration. A perfect catalyst support material should have large surface area, good electrical conductivity and strong interaction between the catalysts [4].

Many ventures have been made to acquire high surface area electrocatalysts to achieve enhanced fuel cell performance using less catalyst loadings. Moreover, the structure of the catalyst support material and their interaction with the metal nanoparticles strongly influence the electrocatalytic performance of a fuel cell. Among various carbon based support materials, graphene and carbon nanotubes are most studied catalyst support material for fuel cell applications due to its fascinating properties like large surface area and high electrical conductivity. However, the high cost of production of these material limits its application in fuel cell. In addition to high production cost, the synthesis of graphene and carbon nanotubes is a multistep process. Therefore, it is necessary to have an efficient catalyst support material which is cost effective and can be produced in a simple way along with high surface area and good electrical conductivity. In this regard, carbon materials derived from conducting polymers appears to be a promising candidate as catalyst support material in fuel cell applications due to its facile and cost effective production compared to graphene and carbon nanotubes. Compared to carbon nanotubes, the tubular polymer derived carbon nanomaterial can be prepared easily in ambient temperature without using highly sophisticated methods in large quantity[11]. Moreover, the polymer derived carbon nanostructures have good electrical conductivity due to the presence of heteroatom nitrogen and high surface area due to its porous structure. In addition, nitrogen doping effectively introduce active sites for nanoparticle dispersion and increases the interaction between catalyst nanoparticles and support material [12]. It has been already proved that pyrolysis of conducting polymers at high temperature is one of the most simple and efficient way to synthesize nitrogen doped carbon nanostructure with required morphology [13,14]. Among the various carbon nanomaterials derived from conducting polymers, one-dimensional nanostructures has gained immense attraction as efficient support material due to its unique hollow 1D nanostructure. Polypyrrole is the most studied material among conducting polymers. For instance, Zhang et al. [15] used polypyrrole nanotubes as advanced support for metal nanoparticle dispersion without surface functionalization. Xu et al. [16] decorated gold nanoparticle over polypyrrole nanotubes prepared by in situ reduction process. Qiu et al. [11] studied the electrocatalytic oxidation of methanol using Pt nanoparticles decorated over polypyrrole nanotubes functionalized with ionic liquid as electrocatalyst. Sapurina et al. [17] has shown that noble metal supported nitrogen doped carbon structure derived from conducting polymers has good catalytic activity.

The present study focuses on the development of non-Pt based electrocatalyst using cost effective support material for both anodic and cathodic reaction in PEMFC. Nitrogen rich carbon nanostructure (NCNS) were prepared by carbonization of polypyrrole nanotubes (PPNT) and was used to disperse Pd_3Co alloy nanoparticles using polyol reduction method. The nitrogen rich catalyst support with tubular morphology and high surface area have significant influence on catalyst nanoparticle dispersion thereby increasing its catalytic performance. The synthesized material was characterized by both physical and electrochemical characterization methods. Thus the evaluation of hydrogen oxidation reaction (HOR) and oxygen reduction reaction (ORR) activity of Pd_3Co/NCNS is reported and compared with the conventional electrodes of a fuel cell.

Experimental

Synthesis of electrocatalyst

Polypyrrole nanotubes (PPNT) were synthesized by the oxidation of pyrrole with ferric chloride ($FeCl_3$) in the presence of a template, methyl orange (MO). The synthesis method is briefly explained as follows. A calculated amount of MO was dissolved in 500 ml of deionized (DI) water followed by the addition of 60 mM $FeCl_3$ solution in to it with continuous stirring. After that, calculated amount of pyrrole was added to the solution in drops. Then, above suspension was allowed to stir for 24 h. The solution was washed several times with dilute hydrochloric acid and DI water till color of the solution changes from dark pink to colorless. Then the product was dried in vacuum oven at 60 ºC to obtain PPNT. The obtained PPNT was pyrolysed in argon atmosphere at 800 ºC for 2 h to form nitrogen rich carbon nanostructure (NCNS). The palladium-cobalt alloy nanoparticles were dispersed over NCNS by well-known polyol reduction method [18]. The schematic representation for the preparation of Pd_3Co/NCNS is shown in Figure 1.

Physical Characterization

XRD patterns were recorded using Rigaku X-ray diffractometer using Cu Kα radiation source at room temperature. Raman spectra were obtained with a Wi-Tec Raman spectrometer in the range of 1000 – 2000 cm^{-1} at room temperature. The morphological and structural analysis of the prepared samples was carried out using scanning electron microscopy (SEM) in Quanta-200 (FEG) and the transmission electron microscopic (TEM) images were recorded using Technai T-20. The nitrogen adsorption/desorption studies to calculate the surface area of the synthesized samples were carried out using Micromeritics ASAP 2020 instrument. The information regarding thermal stability and the amount of metal catalyst loading was obtained from thermogravimetric analysis (TGA) using SDTQ600 TA instruments. X-ray photoelectron spectroscopy (XPS) was carried out to analyze the elemental composition and oxidation state of the elements present using SPECS instrument and it was analyzed using PHOIBOS 100MCD analyzer.

Electrochemical measurements

The electrocatalytic activity of the synthesized samples were studied using cyclic voltammetry (CV), linear sweep voltammetry (LSV), and rotating ring disk electrode (RRDE). All the electrochemical half-cell measurements were carried out using a three electrode electrochemical set up in Biologic SP300 instruments. The working electrode used was a glassy carbon electrode coated with electrocatalyst ink. Platinum rod and saturated calomel electrode (SCE) was used as counter and reference electrode, respectively. All half-cell measurements were carried out in 0.5 M H_2SO_4. Prior to the measurements, the electrocatalyst ink was prepared by dispersing 2.5 mg of electrocatalyst in 150 µl of DI water and 5 µl of 5 wt % of nafion solution. The calculated amount of electrocatalyst ink was drop-casted over well-polished glassy carbon electrode. Same catalyst preparation method was followed for LSV and RRDE measurements to study the ORR activity of the electrocatalysts.

PEMFC single-cell tests

The single-cell measurements were carried out using KPAS fuel cell test station. The electrocatalyst ink was prepared by ultrasonicating the calculated amount of electrocatalyst in a mixture of deionized (DI) water, isopropyl alcohol (IPA) and 5 wt % Nafion solution. The electrodes were prepared by brush coating this ink over a gas diffusion layer (GDL) which is single-sided teflonized carbon cloth (Nickunj Eximp Entp Pvt Ltd, India). After preparing the electrodes, the membrane electrode assembly (MEA) was prepared by sandwiching a polymer membrane (Nafion-212) in between anode and cathode. The MEAs were assembled between the flow field plates made of graphite having serpentine geometry. The effective electrode area was

11.56 cm^2. To control the hydrogen and oxygen gases in electrodes, mass flow controllers were used. The water content in the membrane was maintained using humidifiers, which humidify the incoming hydrogen and oxygen gas to the anode and cathode of the fuel cell.

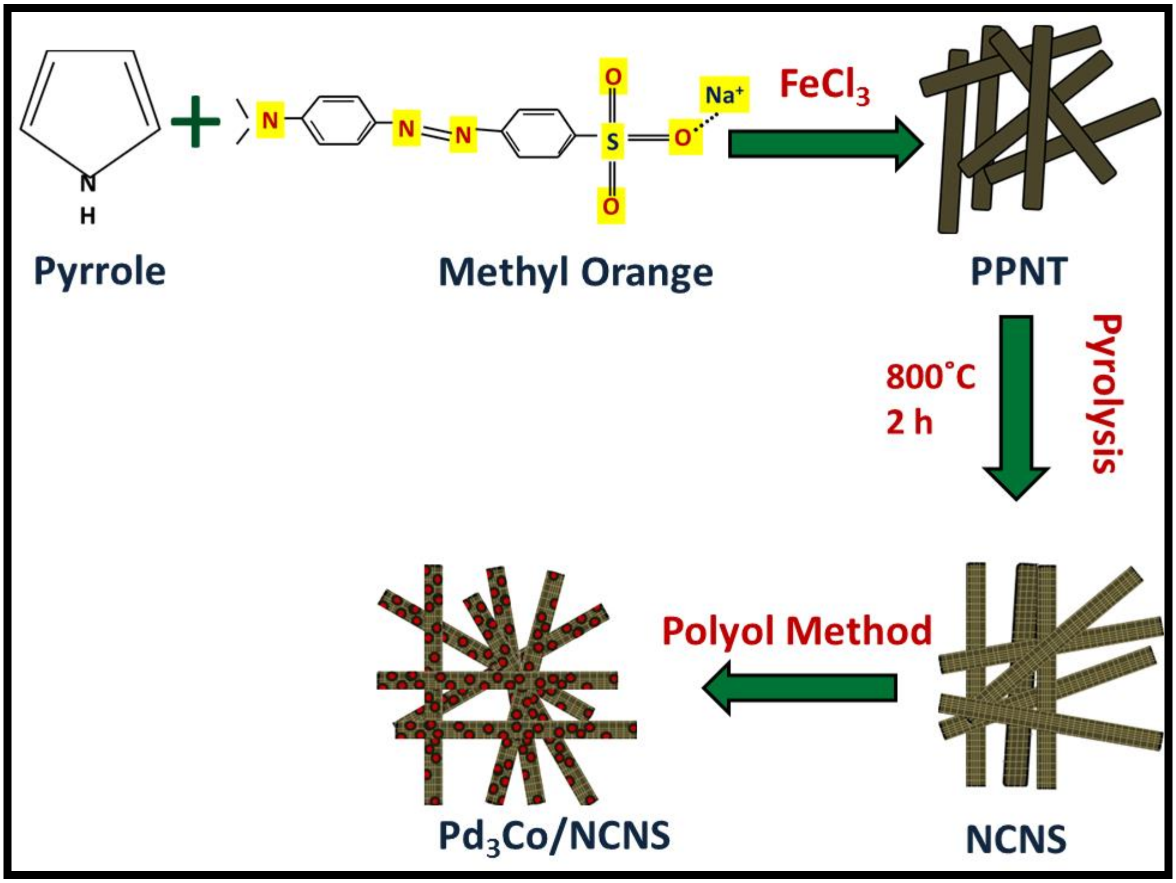

Figure 1: Schematic representation for the preparation of Pd_3Co/NCNS.

Results and discussion

Figure 2 shows the XRD pattern of NCNS, Pd/NCNS and Pd_3Co/NCNS. In Figure 2a, the broad peak centered around 2θ value of 25° can be ascribed to graphite (002) and broadness shows the amorphous nature of PPNT [13]. Along with carbon peak, the peaks centered at 40.02°, 46.53°, 67.97°, 81.93° and 86.44° in XRD pattern of Pd/NCNS can be assigned to the (111), (200), (220), (311) and (222) reflections of palladium, respectively, which in turn confirms the successful deposition of Pd nanoparticles on NCNS. Whereas in case of XRD pattern of Pd_3Co/NCNS, the Pd peaks were shifted to higher angles compared to that of Pd/NCNS (shown in enlarged version of XRD pattern of Pd/NCNS and Pd_3Co/NCNS (Figure 2b), which is due to lattice contraction caused by the addition of small Co atoms. Moreover, no separate signals can be observed corresponding to Co, which further confirms the formation of Pd and Co alloy.

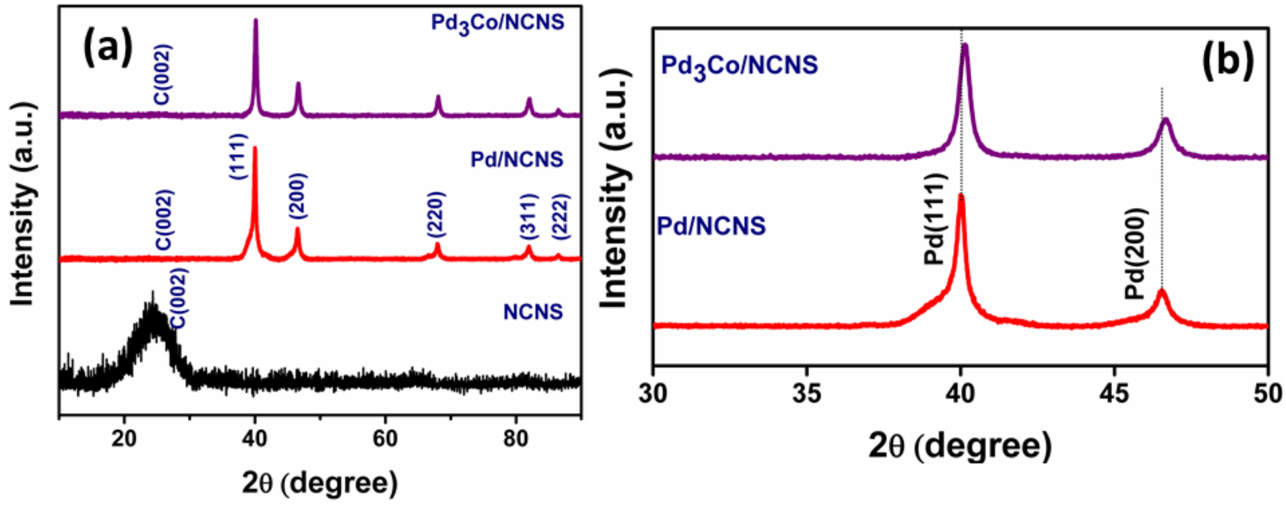

Figure 2: (a) XRD patterns of NCNS, Pd/NCNS and Pd_3Co/NCNS and (b) Enlarged version of XRD patterns of Pd_3Co/NCNS and Pd/NCNS.

The Raman spectra of samples PPNT and NCNS are shown in Figure 3. The Raman spectrum of PPNT does not show clear characteristic peak of graphitic carbon, only displayed the features corresponding to polypyrrole structure. Whereas the spectrum of NCNS shows two sharp bands at 1326 cm^{-1} and 1582 cm^{-1} which corresponds to the D and G bands of graphitic carbon, respectively. The peak at 1326 cm^{-1} is due to the defects present in the carbon structure whereas the peak at 1582 cm^{-1} is due to the vibration of Raman active sp^2 bonded carbon atoms. Thus, the Raman spectra of PPNT and NCNS confirm the formation of carbon materials by pyrolysis of polypyrrole nanotubes.

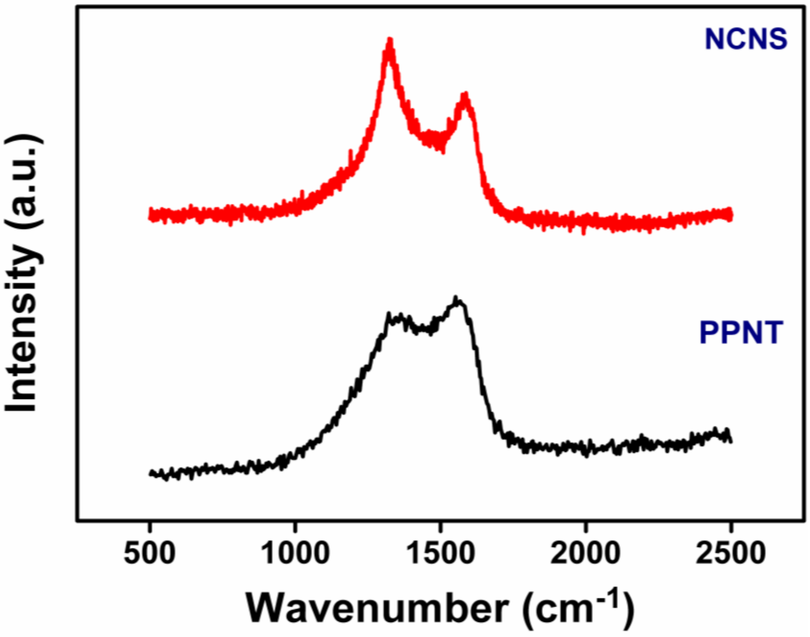

Figure 3: Raman spectra of PPNT and NCNS.

Figure 4 shows the nitrogen adsorption and desorption isotherm for PPNT and NCNS. The BET surface area calculated using BET analyzer is only 38 m^2 g^{-1} for PPNT, whereas with pyrolysis, the specific surface was increased to 220 m^2 g^{-1} for NCNS. Thus, the pyrolysis of the polypyrrole nanotubes at high temperature in Ar atmosphere leads to carbonization and the porous structure was created by the removal of functional groups during the carbonization. Thus the method adopted here to produce nitrogen rich porous carbon structure is very simple. Moreover, the high surface area of NCNS facilitates to improve mass transport in fuel cell.

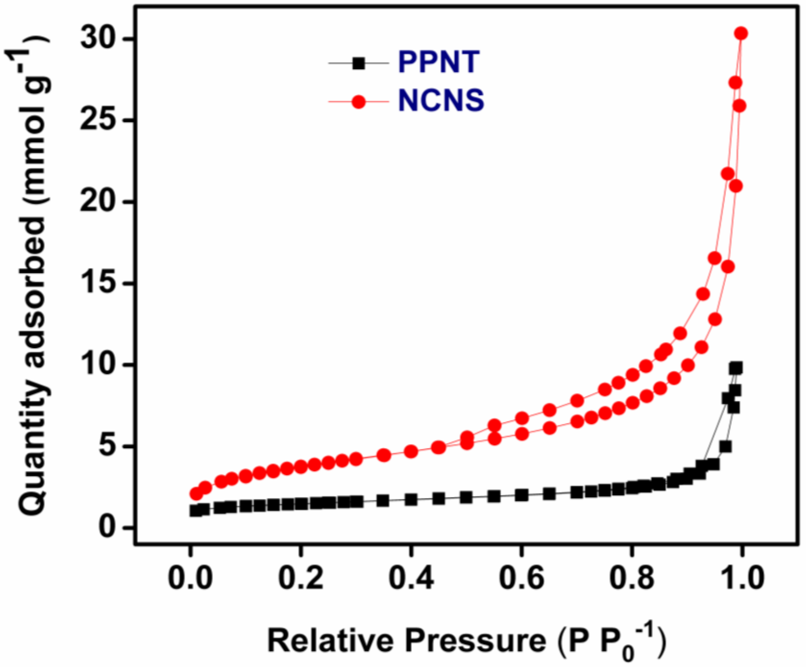

Figure 4: Nitrogen adsorption/desorption isotherm for PPNT and NCNS.

Thermogravimetric analysis was carried out to obtain the information regarding thermal stability of the synthesized materials at zero air atmosphere from room temperature to 800℃. The thermogram of NCNS and Pd_3Co/NCNS in Figure 5 shows an initial loss in weight at lower temperature due to the presence of residual water content present in the samples. Further, the rapid loss in weight observed at a temperature range of 400 – 500℃ is due to the decomposition of carbonaceous species in presence of air. A residual weight of ~ 10 wt% is present in NCNS, which is due to the presence of impurities that is not washed off while filtering the sample. Thus, from the TGA profile of Pd_3Co/NCNS, the presence of ~ 30 wt% of metal catalyst loading can be confirmed.

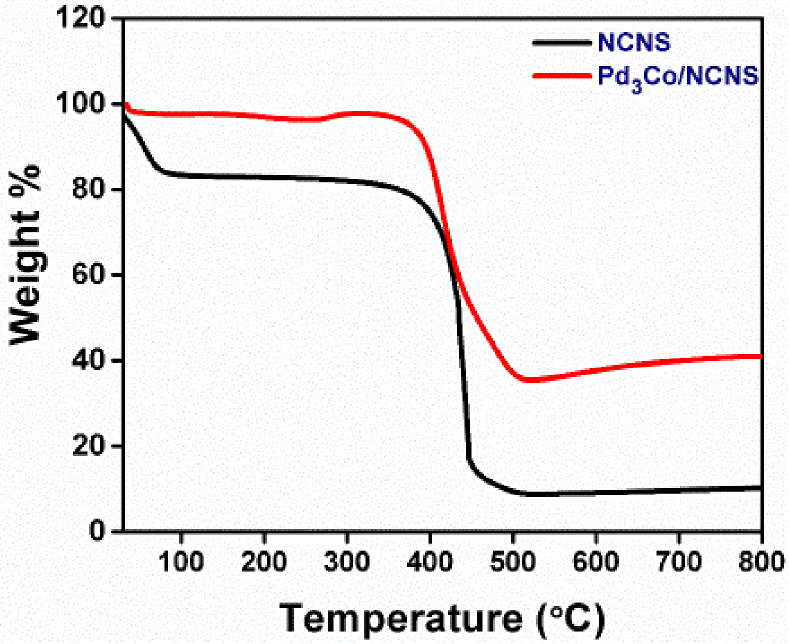

Figure 5: Thermogravimetric curve of NCNS and Pd_3Co/NCNS.

The morphological study of the synthesized samples was carried out using SEM and TEM. Figure 6 (a, b) shows the SEM and TEM images of NCNS which clearly shows the one-dimensional structure of NCNS. Figure 6 (c, d) depicts the SEM and TEM images of Pd_3Co/NCNS which exhibits homogeneous dispersion of uniform sized Pd_3Co nanoparticles on nitrogen rich carbon nanostructures. The homogeneous dispersion of catalyst nanoparticles can be due to more number of nitrogen-carbon moieties present in the support material which acts as active sites. Also, the presence of nitrogen atoms in the carbon structure helps in uniform distribution of catalyst nanoparticles. Moreover, during carbonization, defects were created due to the removal of functional groups which also serve as catalyst anchoring sites. The chemical composition of the synthesized electrocatalyst Pd_3Co/NCNS was determined from the elemental mapping (Figure S1, Supplementary Information). The elemental mapping shows the presence of carbon (C), nitrogen (N), palladium (Pd) and cobalt (Co) in Pd_3Co/NCNS.

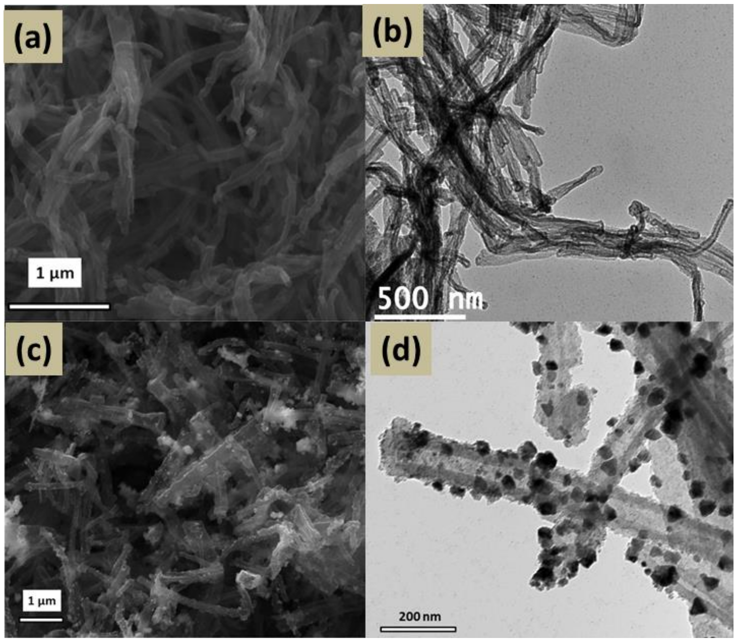

Figure 6: SEM and TEM image (a, b) of NCNS and (c, d) of Pd_3Co/NCNS.

The chemical composition of the prepared electrocatalyst Pd_3Co/NCNS was confirmed by carrying out the X-ray photoelectron spectroscopy (XPS). Figure 7a shows the high resolution XPS spectrum of C 1s orbital. A prominent peak centered at 284.09 eV in the deconvoluted spectrum of C 1s corresponds to sp^2 C=C bonding. Whereas, the two peaks centered at 285.65 eV and 288.09 eV corresponds to the sp^2 C=N and sp^3 C-N bonding, respectively [19]. The deconvoluted spectrum of N 1s shown in Figure 7b consists of three peaks centered at 398.78 eV, 401.07 eV and 406.10 eV corresponds to the pyridinic N, quaternary N, and N-oxide respectively [20,21]. From XPS analysis, the amount of nitrogen atoms doped in the reduced graphene oxide structure was obtained as 4.57 atomic %. Figure 7c shows the deconvulted XPS spectrum of Pd 3d which consists of four peaks. Among four peaks, the peaks centered at 335.65 eV and 341.42 eV correspond to the metallic Pd i.e. Pd^0 $3d_{5/2}$ and Pd^0 $3d_{3/2}$, respectively. Whereas, the other two peaks corresponding to $^+2$ oxidation state of palladium is centered at 337.75 eV (Pd^{+2} $3d_{5/2}$) and at 343.58 eV (Pd^{+2} $3d_{3/2}$) and it is formed due to the formation of Pd-

O bond or Pd-N bond [22] spectrum of Co 2p orbital of Pd_3Co/NCNS is shown in Figure 7d. The two peaks centered around 780.38 eV and 795.39 eV correspond to the Co $2p_{3/2}$ and Co $2p_{1/2}$ respectively [23–25].

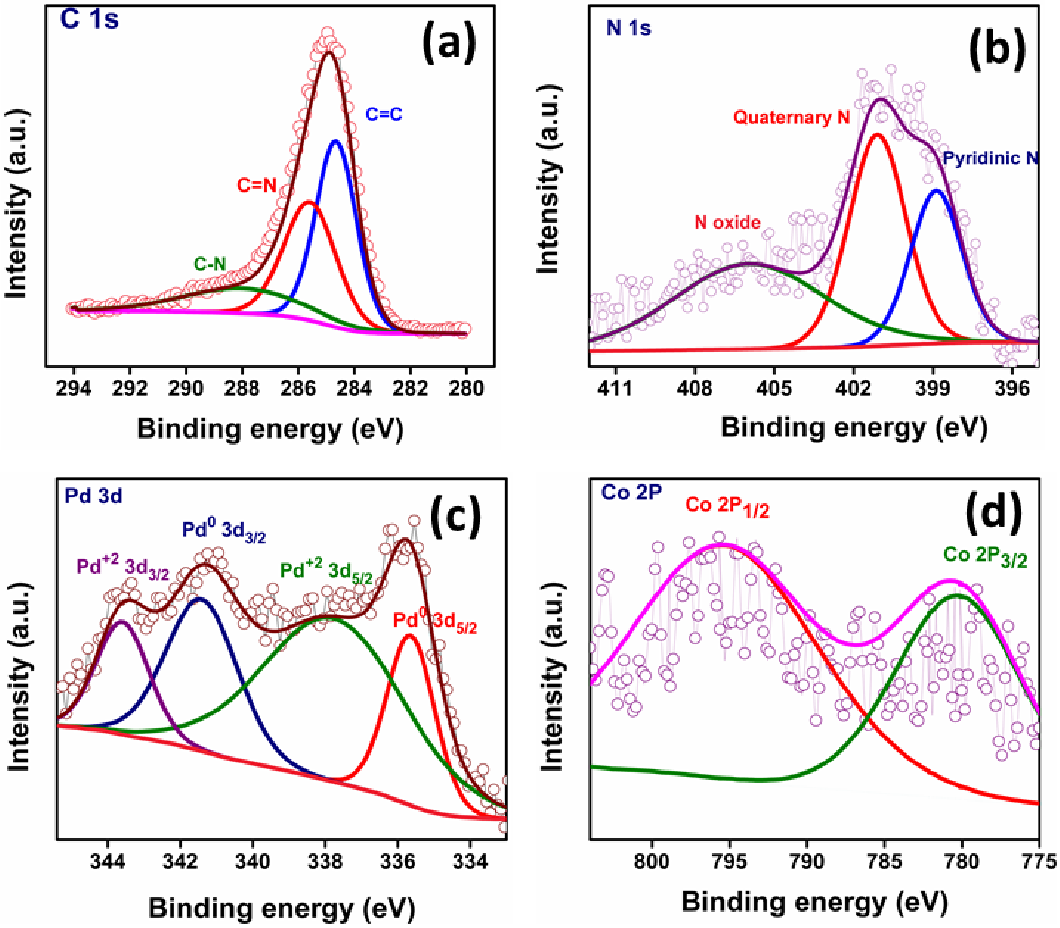

Figure 7: XPS spectra of (a) C 1s, (b) N 1s, (c) Pd 3d and (d) Co 2p orbitals.

The cyclic voltammogram of Pd_3Co/NCNS (Figure 8a) was recorded at a scan rate of 50 mV s^{-1} using saturated calomel electrode (SCE) as reference electrode. The peaks observed between -0.3 V and 0 V corresponds to the hydrogen desorption/adsorption peak. The anodic peak observed above 0.5 V is due to the oxide formation on palladium surface, whereas the cathodic peak observed in the voltage range of 0.45 V to 0.1 V is due to the reduction of Pd oxide to form elemental Pd. Since Pd is hydrogen storage material, the electrochemical surface area (ECSA) was calculated from the Pd-oxide reduction peak using the Equation (1).

$$ECSA = \frac{Q_H}{[M]*Q_M} \tag{1}$$

Where, Q_H is the coulombic charge exchanged during reduction of Pd oxide, Q_M is the adsorption charge for atomically smooth surface area. For Pd, the value of Q_M 0.42 mC cm^{-2} and [M] is the electrocatalyst loading and ECSA is expressed in m^2/g. The ECSA for Pd_3Co/NCNS was obtained to be 82 m^2 g^{-1}. The stability of the electrocatalyst Pd_3Co/NCNS was tested by taking CV measurements before and after 300 cycles (Figure 8b) and it was found that the electrocatalyst is stable without much reduction in current density.

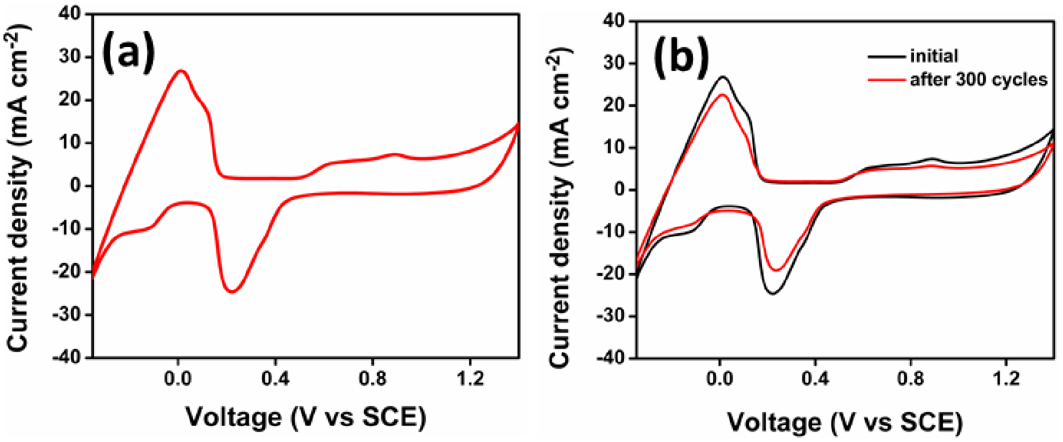

Figure 8: (a) Cyclic voltammogram of Pd_3Co / NCNS and (b) Cyclic voltammogram of Pd_3Co/NCNS before and after 300 cycles.

The RDE measurements were carried out to probe the ORR performance of Pd_3Co/NCNS. Figure 9a depicts the LSV curve of Pd_3Co/NCNS recorded at a scan rate of 5 mV s^{-1} in oxygen saturated 0.5 M H_2SO_4 electrolyte solution at room temperature. To explore the kinetic parameters, the electrode was allowed to rotate in different speeds. From LSV curves, it was observed that the diffusion-limiting current rises with increase in speed of electrode rotation. This can be due to more diffusion of oxygen towards the electrode with increase in rotation rate. From LSV curve, the kinetic parameters related to ORR performance can be found out using Koutecky-Levich (K-L) plot using K-L Equation (2).

$$\frac{1}{j}=\frac{1}{j_k}+\frac{1}{j_d}=\frac{1}{nFkC_{O_2}}+\frac{1}{B\omega^{1/2}} \qquad (2)$$

where,

$$B=0.2nFC_{O_2}D_{O_2}{}^{2/3}\nu^{-1/6} \qquad (3)$$

where j, j_k and j_d is the experimentally measured current density, kinetic current density and diffusion-limited current density, respectively. The electrode rotation speed (ω) is expressed in rpm, k is the rate constant, F is the Faraday constant (96486 C mol^{-1}), n is the electron transfer number per molecule of oxygen in ORR, D_{O_2} is the oxygen diffusion coefficient in electrolyte (1.4×10^{-5} cm^2 s^{-1}), υ is the kinematic viscosity of the electrolyte (1×10^{-2} cm s^{-1}) and C_{O_2} is the concentration of oxygen in the electrolyte (1.1×10^{-6}mol cm^{-3}) in 0.5 M H_2SO_4 [26,27]. The constant B in Equation (3) can be obtained from K-L plots (j^{-1} vs $\omega^{-1/2}$), from which the electron transfer number (n) involved in ORR process can be calculated. Figure 9b shows the K-L lines of Pd_3Co/NCNS at different potentials along with the theoretical line for two electron (n =2) and four electron (n = 4) process. It can be seen that the experimental K-L lines are almost parallel to each other as well as to the theoretical n = 4 K-L line. Further, the n value calculated from slope of the experimental K-L lines was found to be approximately 3.56. This suggests the ORR catalyzed by Pd_3Co/NCNS was via nearly four-electron transfer mechanism. The LSV curve of Pd_3Co/NCNS at 1600 rpm electrode rotation speed was compared with that of Pd_3Co decorated over another 1D carbon nanostructure, multiwalled carbon nanotubes (CNT) [18] and commercial Pt/C [28] (Figure S2). It was observed that the Pt/C shows better ORR activity than that of Pd-alloy based electrocatalysts. Whereas among Pd-based electrocatalysts, the onset potential of Pd_3Co/NCNS was better compared to Pd_3Co/CNT which is an indication of improved catalytic activity of Pd_3Co/NCNS.

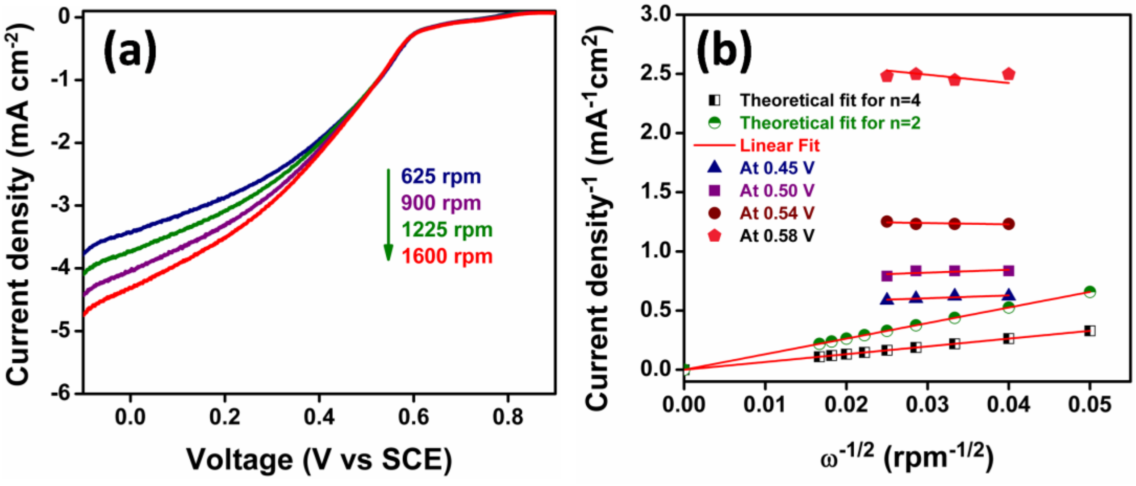

Figure 9: (a) LSV curve of Pd_3Co/NCNS at different electrode rotation speed and (b) Koutecky-Levich plot of Pd_3Co/NCNS.

Further, for gathering more accurate information regarding the ORR reaction pathway, RRDE measurements were performed. Figure 10a shows the RRDE curve of Pd_3Co/NCNS at 1600 rpm with 5 mV s^{-1} scan rate. The percentage amount of hydrogen peroxide (H_2O_2) produced and the electron transfer number (n) during the ORR mechanism was calculated using the Equation (4) and (5) [12].

$$\%H_2O_2 = \frac{200i_r / N}{i_d + i_r / N} \tag{4}$$

$$n = \frac{4i_d}{i_d + i_r / N} \tag{5}$$

where i_r is the ring current, i_d is the disk current and N is the collection efficiency (0.37).

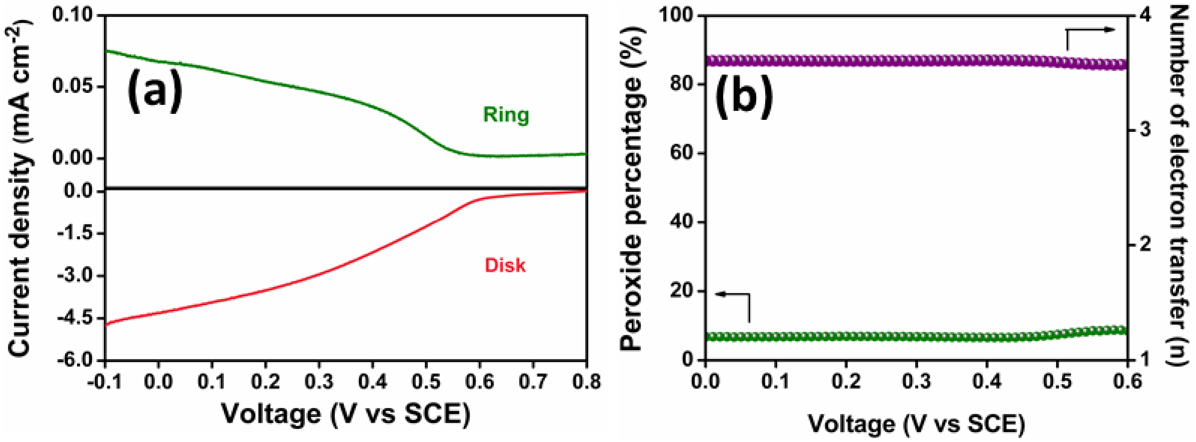

Figure 10: (a) RRDE curves of Pd_3Co/NCNS at 1600 rpm and (b) Percentage of hydrogen peroxide produced and electron transfer number during ORR of Pd_3Co/NCNS.

The amount of hydrogen peroxide produced and electron transfer number during ORR by the electrocatalyst Pd_3Co/NCNS is shown in Figure 10b. The percentage of peroxide produced varies from 6 % to 10 % in the potential range 0 V to 0.6 V. The calculated number of electrons transferred during the ORR mechanism from RRDE was found to vary from 3.58 to 3.62 in the potential range 0 V to 0.6 V vs SCE. Thus, Pd_3Co/NCNS is a promising electrocatalyst for ORR which follows nearly four electron pathway.

The fuel cell performance studies were carried out by preparing MEA 1using Pd_3Co/NCNS as anode electrocatalyst with commercial Pt/C as cathode and were labeled as MEA 1. Similarly, MEA 2 was prepared by reversing anode and cathode. In addition to it, MEA 3 was prepared using Pd_3Co/NCNS at both anode and cathode. The catalyst loading of Pd_3Co/NCNS was 0.5 mg cm^{-2} and that of commercial Pt/C was 0.1 mg cm^{-2}. Figure 11 (a-c) shows the polarization curves of MEA 1, MEA 2 and MEA 3 at three different temperatures 40 °C, 50 °C and 60 °C, respectively.

Prior to the polarization studies, the electrodes were activated between open circuit potential and 0.1 V. Using MEA 1, the maximum power density of 374 mW cm^{-2} was obtained at 60 °C. Similarly, in case of MEA 2, the peak power density of 257 mW cm^{-2} was achieved. The maximum power density of Pd_3Co/NCNS as cathode electrocatalysts at 60 ° C without back pressure is higher than the performance of previously reported Pd based electrocatalysts [29–31]. The MEA 3 which is completely free from Pt showed maximum power density of 129 mW cm^{-2} at 60 ° C, which is a very good performance without Pt on either electrode.Pd_3Co/NCNS showed enhanced performance compared to other similar reported work from our group, using same catalyst alloy nanoparticles over different catalyst support materials with same catalyst metal loading [18,28]. For comparison, another MEA was prepared and tested using Pd/NCNS as both anode and cathode electrocatalyst, and the maximum power density obtained at 60 ° C was 102 mW cm^{-2} (Figure S3). The fuel cell performance of Pd_3Co/NCNS is further compared with the performance of commercial Pt/C and shown in Figure S4 [18]. The maximum power density value obtained using commercial Pt/C with 0.1 mg cm^{-2} catalyst loading on both sides was 515 mW cm^{-2}. The peak power density attained using Pd_3Co/NCNS at anode, cathode and at both electrodes showed almost 73 %, 50 % and 25 % of maximum power density attained using commercial Pt/C on both sides, respectively. Thus, the achievement of almost 25 % of maximum power density of that of commercial Pt/C catalyst is the best value obtained so far using non-Pt based electrocatalyst on both sides of a fuel cell. The maximum power density values obtained using different MEAs at 60 ° C are given in Table 1. The enhanced performance of Pd_3Co/NCNS can be attributed to the presence of more number of N-C moieties present in NCNS which acts as active catalyst sites and improved electrical conductivity due to the presence of nitrogen in addition to alloying effect. Moreover, nitrogen doping enhances the interaction between catalyst nanoparticle and support material. In addition, the high surface area with porous nature of NCNS helps in easy mass transfer thereby improving HOR and ORR.

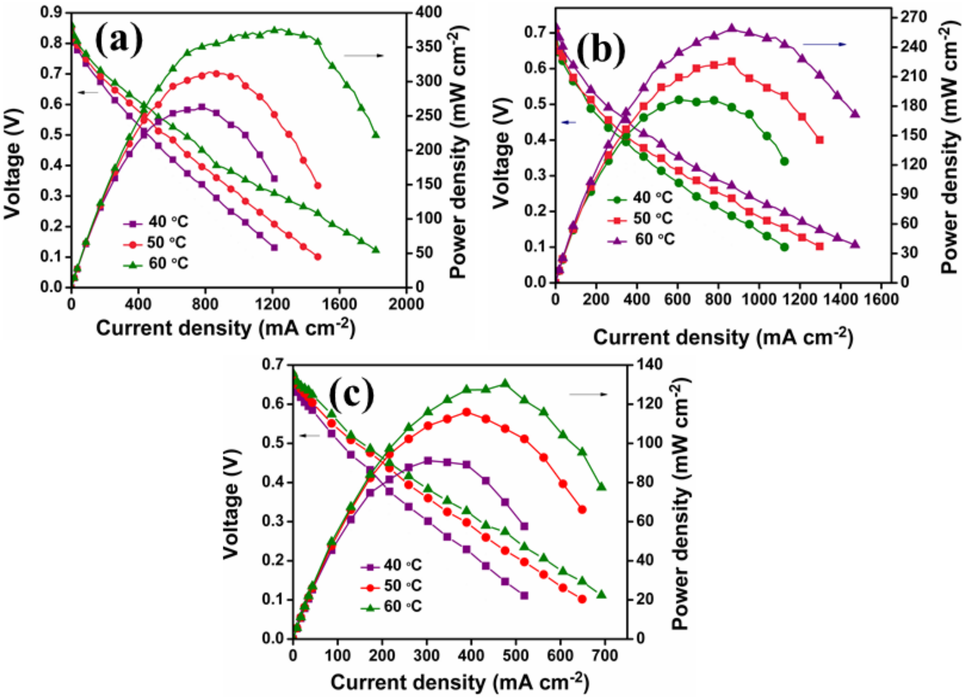

Figure 11: Polarization curves of (a) Pd_3Co/NCNS as anode electrocatalyst, (b) Pd_3Co/NCNS as cathode electrocatalyst and (c) Pd_3Co/NCNS as both anode and cathode electrocatalyst at 40 ° C, 50 ° C and 60 ° C temperature.

Table 1. Maximum power density obtained for different MEA's at 60 ° C temperature with Pt/C loading of 0.1 mg cm^{-2} and Pd_3Co/NCNS loading of 0.5 mg cm^{-2}.

Sl.No.	Anode	Cathode	Maximum Power density at 60 ° C (mW cm^{-2})
1.	Pd_3Co/NCNS	Pt/C	374
2.	Pt/C	Pd_3Co/NCNS	257
3.	**Pd_3Co/NCNS**	**Pd_3Co/NCNS**	**129**
4.	Pd/NCNS	Pd/NCNS	102

Conclusion

Nitrogen rich carbon nanostructure derived from conducting polymer was successfully synthesized and employed as an efficient catalyst support material in PEMFC due to its facile and cost effective production compared to commonly used carbon nanomaterials like graphene and carbon nanotubes. Palladium-cobalt alloy based nanocomposite was prepared using NCNS as catalyst support material. Both half-cell and single-cell measurements were carried using as-synthesized nanocomposite. RDE and RRDE measurements showed that the ORR mechanism in Pd_3Co/NCNS proceeds via nearly four electron pathway. The peak power density achieved using Pd_3Co/NCNS at both anode and cathode simultaneously was almost 25 % of the maximum power density attained using commercial Pt/C on both sides. The superior performance of Pd_3Co/NCNS is attributed to the presence of more number of N-C moieties in NCNS which acts as active catalyst sites and improved electrical conductivity due to the presence of nitrogen. In addition, high surface area of hollow porous structure helps in easy mass transfer thereby improving HOR and ORR. Thus Pd_3Co/NCNS has proved to be a promising cost-effective non-Pt anode and cathode electrocatalyst in PEMFC with excellent catalytic performance.

Acknowledgements

Authors thank Indian Institute of Technology Madras for the financial support.

References

1. Takigami, M.; Kobayashi, R.; Ishii, T.; Imashiro, Y.; Ozaki, J.I. *Beilstein J. Nanotechnol.* **2019**, 10,1391–1400. doi:10.3762/bjnano.10.137

2. Louisia, S; Thomas, R.J.Y.; Lecante, P.; Heitzmann, M.; Axet, M.R.; Jacques, P.; Serp, P. *Beilstein J. Nanotechnol.* **2019**, 10, 1251–1269. doi:10.3762/bjnano.10.125

3. Deng, R.; Xia, Z.; Sun, R.; Wang, S.; Sun, G. *J. Energy Chem.* **2020**, *43*, 33–39. doi:10.1016/j.jechem.2019.07.015

4. Vinayan, B.P.; Nagar, R.; Rajalakshmi, N.; Ramaprabhu, S. *Adv. Funct. Mater.* **2012**, *22*, 3519–3526. doi:10.1002/adfm.201102544

5. Zhang, Z.; Liu, S.; Tian, X.; Wang, J.; Xu, P.; Xiao, F.; Wang, S. *J. Mater. Chem. A* **2017**, 1–9. doi:10.1039/c7ta00710h

6. Qi, Y.; Wu, J.; Zhang, H.; Jiang, Y.; Jin, C.; Fu, M.; Yang, H.; Yang, D. *Nanoscale* **2014**, *6*, 7012. doi: 10.1039/c3nr06888a

7. Savadogo, O.; Lee, K.; Oishi, K.; Mitsushima, S.; Kamiya, N.; Ota, K.I. *Electrochem. commun.* **2004**, *6*, 105–109.doi: 10.1016/j.elecom.2003.10.020

8. Wang, D.; Xin, H.L.; Wang, H.; Yu, Y.; Rus, E.; Muller, D.A.; Disalvo, F.J.; Abruña, H.D. *Chem. Mater.* **2012**, *24*, 2274–2281.doi: 10.1021/cm203863d

9. Savadogo, O.; Varela, F.J.R. *J. New Mater. Electrochem. Syst.* **2008**, *11*, 69–74. doi: 10.1149/1.2214495

10. Takenaka, S.; Tsukamoto, T.; Matsune, H.; Kishida, M. *Catal. Sci. Technol.* **2013**, *3*, 2723.doi: 10.1039/c3cy00446e

11. Qiu, L.; Liu, B.; Peng, Y.; Yan, F. *Chem. Commun.* **2011**, *47*, 2934–2936. doi: 10.1039/c0cc04865h

12. Bau, Vincent Mirai Bo, Xiangjie Guo, L. *J. Energy Chem.* **2017**, 26, 63–71. doi: 10.1016/j.jechem.2016.07.005

13. Puthusseri, D.; Ramaprabhu, S.. *Int. J. Hydrogen Energy* **2016**, *41,* 13163–13170. doi: 10.1016/j.ijhydene.2016.05.146

14. Shrestha, S.; Mustain, W.E. *J. Electrochem.Soc.* **2010**,157, B1665-B1672. doi: 10.1149/1.3489412

15. Zhang, J.; Liu, X.; Zhang, L.; Cao, B.; Wu, S. *Macromol. Rapid Commun*.**2013**, 34, 528–532. doi: 10.1002/marc.201200757

16. Xu, J.; Hu, J.; Quan, B.; Wei, Z. *Macromol. Rapid.Commun.* **2009**, *30,* 936–940.doi: 10.1002/marc.200800764

17. Trchova, M.; Kopecka, J.; Cieslar, M.; El-nasr, A.A.; Ayad, M.M. *Synth. Met.* **2016**, *214*, 14–22.doi: 10.1016/j.synthmet.2016.01.009

18. Chandran, P.; Ramaprabhu, S. *Int. J. Hydrogen Energy* **2018**, 43, 1–11.doi: 10.1016/j.ijhydene.2018.08.066

19. Shende, R.; Sundara, R. *Sol. Energy Mater. Sol. Cells* **2015**, *140*, 9–16. doi: 10.1016/j.solmat.2015.03.012

20. Wickramaratne, N.P.; Xu, J.; Wang, M.; Zhu, L.; Dai, L.; Jaroniec, M. *Chem. Mater.* **2014**, *26*, 2820–2828. doi: 10.1021/cm5001895

21. Li, Z.; Gao, Q.; Zhang, H.; Tian, W.; Tan, Y.; Qian, W.; Liu, Z. *Sci. Rep.* **2017**, *7*, 1–9. doi: 10.1038/srep43352

22. Qiu, X.; Zhang, H.; Dai, Y.; Zhang, F.; Wu, P.; Wu, P.; Tang, Y. *Catalysts* **2015**, *5*, 992–1002. doi: 10.3390/catal5020992

23. Kuang, M.; Li, T.T.; Chen, H.; Zhang, S.M.; Zhang, L.L.; Zhang, Y.X. *Nanotechnology* **2015**, *26*, 1–9. doi: 10.1088/0957-4484/26/30/304002

24. Kocijan, A.; Milošev, I.; Pihlar, B. *J. Mater. Sci. Mater. Med.* **2004**, *15*, 643–650.doi: 10.1023/B:JMSM.0000030204.0861

25. Huang, J.; Qian, W.; Ma, H.; Zhang, H.; Ying, W. *RSC Adv.* **2017**, *7*, 33441–33449.doi: 10.1039/c7ra05887j

26. Chandran, P.; Puthusseri, D.; Ramaprabhu, S. *Int. J. Hydrogen Energy* **2019**, *44*, 4951–4961.doi: 10.1016/j.ijhydene.2018.12.209

27. Zhang, L.; Qi, C.; Zhao, A.; Xu, G.; Xu, J.; Zhang, L. *Appl Surf Sci.* **2018**, *445*, 462–470. doi: 10.1016/j.apsu sc.2018.03.145

28. Chandran, P.; Ghosh, A.; Ramaprabhu, S. *Sci. Rep.* **2018**, *8*, 3591. doi: 10.1038/s41598-018-22001-9

29. Moreira, J.; Del Angel, P.; Ocampo, A.L.; Sebastián, P.J.; Montoya, J.A.; Castellanos, R.H. *Int. J. Hydrogen Energy* **2004**, *29*, 915–920. doi: 10.1016/j.ijhydene.2003.06.003

30. Martinez-Casillas, D.C.; Vazquez-Huerta, G.; Perez-Robles, J.F.; Solorza-Feria, O. *J. Power Sources* **2011**, *196*, 4468–4474.doi: 10.1016/j.jpowsour.20111.01.050

31. Martínez-Casillas, D.C.; Calderon, H.A.; Collins-Martínez, V.; Solorza-Feria, O. *Int. J. Hydrogen Energy* **2013**, *38*, 12674–12680.doi: 10.1016/j.ijhydene.2012.11.066